Twinning anisotropy of tantalum during nanoindentation

Twinning anisotropy of tantalum during nanoindentation

Saurav Goel[a*], Ben Beake[b,c], Chi-Wai Chan[a], Nadimul Haque Faisal[d] and Nicholas Dunne[a]

[a]*School of Mechanical and Aerospace Engineering, Queen's University, Belfast, BT9 5AH, UK*

[b]*Micro Materials Limited, Willow House, Yale Business Village, Ellice Way, Wrexham, LL13 7YL, UK*

[c]*Dalton Research Institute, Manchester Metropolitan University, Manchester, M15GD, UK*

[d]*School of Engineering, Robert Gordon University, Garthdee Road, Aberdeen, AB10 7GJ, UK*

*Corresponding author Tel.: +44-28-90975625, Email address: S.GOEL@qub.ac.uk, Fax: +44-28-90974148

Abstract:

Unlike other BCC metals, the plastic deformation of nanocrystalline Ta during compression is regulated by deformation twinning. Whether or not this twinning exhibits anisotropy was investigated through simulation of displacement-controlled nanoindentation test using molecular dynamics simulation. MD data was found to correlate well with the experimental data in terms of surface topography and hardness measurements. The mechanism of the transport of material was identified due to the formation and motion of prismatic dislocations loops (edge dislocations) belonging to the 1/2<111> type and <100> type Burgers vector family. Further analysis of crystal defects using a fully automated dislocation extraction algorithm (DXA) illuminated formation and migration of twin boundaries on the (110) and (111) orientation but not on the (010) orientation and most importantly after retraction all the dislocations disappeared on the (110) orientation suggesting twinning to dominate dislocation nucleation in driving plasticity in tantalum. A significant finding was that the maximum shear stress (critical Tresca stress) in the deformation zone exceeded the theoretical shear strength of tantalum (Shear modulus/ 2π~10.03 GPa) on the (010) orientation but was lower than it on the (110) and the (111) orientations. In light to this, the conventional lore of assuming the maximum shear stress being 0.465 times the mean contact pressure was found to break down at atomic scale.

Keywords: MD simulation; Nanoindentation; Tantalum; Anisotropy.

Abbreviations:

BCC	Body centred cubic
CAT	Crystal analysis tool
COMB	Charge optimized many body potentials
DFT	Density-functional theory
DXA	Dislocation extraction algorithm
EAM	Embedded-atom-method
FCC	Face centred cubic
GB	Grain boundary
MD	Molecular dynamics
NVE	Microcanonical ensemble
OVITO	Open Visualization tool
PBC	Periodic boundary condition
ReaxFF	Reactive Force field
TRISE	Temperature and rate indentation size effect
VMD	Visual molecular dynamics

Nomenclatures:

a	Contact radius of the spherical indenter
A	Projected area
b	Direction of Burgers vector
B	Bulk modulus
C_i	Elastic constants of the material
D	Grain size
E or E_s	Bulk elastic modulus of the material
E_{Shape}	Size dependent Young's modulus of the material
F or P	Normal force or load on the indenter
G	Shear modulus
h	Instantaneous displacement of the indenter
h_f	Residual depth of indentation
h_{max}	Maximum depth of indentation
H	Bulk hardness of the material
Hs	Size dependent hardness
K_{Hx}	Coefficients of a parabolic relationship between hardness and $D^{-1/2}$
L	Total length of dislocations in Å
P-h	Load-displacement curve
p_m	Mean pressure (force / projected area)
R	Radius of the indenter
R_{pl}	Radius of the plastic zone
S	Slope of the unloading curve (Stiffness)
Ta	Tantalum
$\sigma_{hydrostatic}$	Hydrostatic stress
σ_{Tresca}	Tresca Stress or Maximum shear stress
σ_1, σ_2 and σ_3	Principal stresses in three dimensions
σ_y	Size dependent yield stress
σ_0	Bulk yield stress
ε	Strain
τ	Shear stress

1. Introduction

Tantalum, a BCC metal and a part of refractory metal group is a candidate material for applications in bio-medical industries, high-temperature hardware and in the electronics industry partly also because of its very high melting point (3290K) which is exceeded only by rhenium (3453K) and tungsten (3683K) thereby allowing to study the BCC peculiarities of Ta at room temperature (BCC metals typically shows a BCC-type and FCC-type behaviours at about 0.15 $T_{melting}$ ~ 493.5 K for tantalum) [1]. Hence, there is a surge of interest in advancing the current understanding on the deformation mechanics of tantalum.

Awareness of the nanoscale mechanical properties and the mode of deformation of metallic materials (BCC metals in particular) is of particular interest to several disparate disciplines including materials science, applied physics, solid state physics, geophysics as well as planetary physics. In this context, whilst nanoindentation differs from nanometric cutting as the former is dominated by compression rather than shear, it enables generating the conditions of high hydrostatic pressure [2], which in turn facilitates studying fundamental reasons of incipient plasticity. Since first being proposed by Hertz in 1881, contact mechanics theory has undergone numerous extensions incorporating anisotropic heterogeneous media along with changes in indenter shape. The most widely studied example of contact loading conditions, nanoindentation testing, has become an indispensable tool in characterizing a range of materials. Nanoindentation of metals in particular, involves plastic deformation due to several competing mechanisms such as nucleation and motion of dislocations, deformation twinning and grain boundary sliding (a subset of slip mechanics) [3].

A notable feature of plasticity in BCC metals is their asymmetry in tension-compression behaviour [4] and this asymmetry has been attributed to the differences in the different deformation mechanisms i.e. dislocation glide prevails in compression while twinning is prominent during tensile pulling of BCC metals. An exception to this observation has recently come from recent experiments [5], where unlike other BCC metals, the plastic deformation of Ta during its nanoindentation was found to be dominated by the deformation twinning. Another area where Ta

has shown deviation from the classical knowledge is that its elastic-plastic transition on the (110) crystallographic direction occurs beyond the theoretical critical value of shear stress [6], thereby pointing to the fact that the parameter critical resolved shear stress may not be applicable at atomic scale where the role of dislocation mechanics is more prevalent. This has in fact now been clarified that at atomic scale, a more fundamental criterion for nucleation of plastic deformation is that the work done over the displaced surface should be greater than the line energy of the new dislocation loop [7] and hence an understanding of the dislocation mechanics is important. These observations should not be surprising considering the fact that Ta does not obey the Schmidt law. In this regard, the current pool of knowledge on the deformation behaviour of Ta is still sparse [5]. Surveying the wealth of reported literature on Ta, the following questions have still not been answered:

1. Whether the maximum shear stress during plastic deformation of Ta exceeds the theoretical shear strength on all crystal planes or just one particular plane?
2. What is the critical magnitude of the stress (von Mises, Tresca, Principal stresses) that causes nanoscale yielding in tantalum on the three principal orientations?
3. What is the fate of crystal twinning upon retraction of the load?
4. Does the crystal twinning in tantalum during nanoindentation is common to all crystal planes or is this observable only on selected crystal planes? If so, does the effect of twinning during unloading shows the same anisotropic behaviour as it is observed during loading?

In pursuit of an answer to these questions, the MD simulation in this work was carried out as a substitute to potentially time consuming and costly experiments which would not permit the precise and real time monitoring of all the atomic scale processes. Exploration of such sort will help improve the design of tantalum material for various engineering applications and will simultaneously help enhance our overall understanding of this notorious BCC material which deviates in its deformation behaviour from other BCC materials.

2. Literature review

Following a brief discussion on the crystallography of Ta, this section presents a brief review of the literature on the atomic structure, structure-property relationship and mechanical response of

Ta under several types of deformation processes such as nanoindentation, uniaxial tension and uniaxial compression.

In nature, tantalum exists in either the BCC alpha phase (α-Ta) or the metastable-tetragonal beta phase (β-Ta). α-Ta is the phase commonly found in bulk tantalum (ductile), and exhibits higher ductility but lower resistivity and hardness than β-Ta (brittle) [8]. In a magnetron sputtering study of Ta films, Myers *et al.* [9] reported that the β to α transition occurs between the temperature 638 K and 648 K. Knepper *et al.* [10] also had similar observations and indicated that β-Ta is no longer favourable when temperatures reaches in the range of 613 K to 623 K. Bulk Ta (α-Ta) resides in a BCC crystal structure and hence analysing its crystallography is rather straightforward. The closed packed planes and closed-packed directions in a BCC crystal have important implications on the deformation behaviour of the material. It is significant in most cases that if the atomic density per unit area is highest on any crystal orientation and the distance between the two adjacent planes is farthest, then this becomes the weaker plane and is more amenable to deformation [11]. To aid to this aspect, an analytical exercise was performed to evaluate the planar density (number of atoms/ unit atomic area) and linear atomic density (number of atoms per unit atomic length) to identify the closed pack planes and directions in tantalum as shown schematically in figure 1. In conjunction with figure 1, table I provide the quantitative details of the number of atoms on a particular crystal plane, atomic projection area, planar density of atoms on each plane, linear atomic density of atoms along each direction and distance between two adjacent crystallographic of Ta.

Table I: Variation in the properties of Ta with respect to various crystal orientations

	Number of atoms on the plane (m)	Atomic projection area (n)	Planar density (Planar) (number of atoms / Å^2)	Linear atomic density (Direction) (number of atoms/ Å)	Distance between two adjacent planes
Cube (010)	$\frac{1}{4}\times 4 = 1$	a×a =a^2	1/a^2 =0.0916	1/a =0.3027 Å	a = 3.304 Å
Dodecahedron (110)	$\left(\frac{1}{4}\times 4\right)+1=2$	√2a×a $=\sqrt{2}a^{2}$	2/√2a^2 **=0.1295**	1/√2a =0.214 Å	√2a = **4.67 Å**
Octahedron (111)	$\frac{1}{6}\times 3=\frac{1}{2}$	$\left(\frac{1}{2}\sqrt{2}a\right)\times\sqrt{\frac{3}{2}}a$ $=\frac{\sqrt{3}}{2}a^{2}$	$\frac{1}{2}\Big/\frac{\sqrt{3}}{2}a^{2}$ =1/√3a^2 = 0.0529	2/√3a =**0.3495 Å**	0.577a = 1.906 Å

a = lattice constant of Ta is considered as 3.304 Å as per EAM potential used in this study.

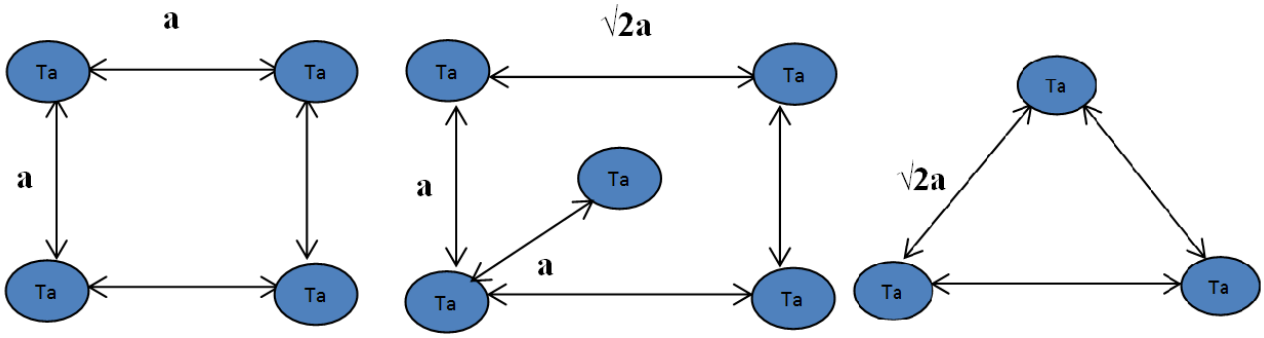

(a) (010) orientation **(b) (110) orientation** **(c) (111) orientation**

Figure 1: Schematic illustration of various crystal orientations in tantalum.

It can be seen from Table I that the distance between the two atomic planes is maximum on the (110) plane and minimum on the (111) plane. This implies that the Peierls stress (0.02-0.03 times the bulk shear modulus of Ta) required to move a dislocation on the (110) plane of BCC will decrease while on the (111) plane would increase. The maximum value of linear atomic density in Table I signifies the closed packed direction in the crystal whereas analogous to this i.e. planar density signifies closely-packed planes in a crystal. Accordingly, it is also evident from Table I that in tantalum (akin to other BCC materials) the (110) plane has high planar atomic density (analogous to close-packed planes) and the <111> are closest-packed directions. What is also known from the literature is that since it requires lower magnitude of energy/ shear stress for slip on densely closed packed planes,

slip in BCC material should occur preferentially on the (110) planes along the <111> direction. However, it may be noted that at low temperature, the slip system in tantalum is <112> direction on the (110) plane [12].

With this theoretical knowledge, a myriad of studies have been done to study the deformation behaviour of α-Ta as a model BCC system. Recent research shows that the plastic deformation in tantalum start with twins, which transforms to shear loops and eventually to prismatic loops whereby the screw components of the shear loop cross-slip and pinch out a prismatic loop in a "lasso" action [13]. Biener *et al.* [1] performed nanoindentation experiments on the (010), (110) and (111) orientation of single crystal Ta to characterise the dislocation nucleation phenomenon, and their results indicated that single pop-in behaviour characteristic can be observed for the (001) orientation, but multiple pop-ins were observed on the (110) and (111) orientations. Attributing this as a general trend to all the BCC materials, they speculated that the (010) orientation of Ta is a typical example of surface which shows dislocation multiplication process, i.e. once plasticity starts, the material flows continuously and no further pop-ins are observed. Guerrero *et al.* [6] carried out MD simulation of uniaxial compression of nanocrystalline tantalum using their *in-house* developed EAM potential function to study the elastic-plastic transition on three crystallographic directions namely, (100), (110) and (111). They monitored the variation of phonon with respect to the applied strain rate and based on this, they concluded that the nucleation of defects along (110) of Ta was due to crystal twinning arising out of dynamical instabilities (soft phonons). They also discovered that the critical stress causing the elastic-plastic transition on the (110) crystallographic direction exceeds the theoretical critical value of shear stress of Ta.

α-Ta films with grain size of 10 to 30 nm prepared on oxidised silicon substrate by magnetron sputtering were recently investigated using nanoindentation [5] with a Berkovich indenter. It was found out that the plastic deformation of nanocrystalline Ta during nanoindentation is due to the crystal twinning (the location of twins being near to the edges and corners of the indent) with the threshold density limit of twins being 4×10^7 per metre resulting in a total strain of about 3.7% [5]. This finding was in contrast to a common lore whereby shear banding is considered

to be the prevalent mechanism during the deformation of BCC metals. This couples further with the work of Tang *et al.* [14] who observed an inverse Hall-Petch relationship in Ta between the compressive yield stress and grain size in the range between 2.5 nm and 30 nm thus adding further mystery to the scenario. They performed MD simulation of uniaxial loading using the extended Finnis-Sinclair potential to simulate the grain boundary configurations of nanocrystalline Ta, and their results revealed that such a system behaved differently when subjected to tensile and compressive loading conditions. The critical grain size for the transition from grain-boundary plasticity to dislocation plasticity reported by them was 20 nm. A similar observation came from the work of Cao *et al.* [8] who performed nanoindentation experiments on the nanocrystalline β-Ta film (prepared by magnetron sputtering on the (111) surface of the silicon substrate). Their results indicated that the nanoindentation hardness decreases with decreasing grain size (inverse Hall-Petch relationship) at a finite scale of 10-20 nm. Noticeably, the nanoindentation hardness and elastic modulus (at a strain rate of $1s^{-1}$) obtained by them were about 18 GPa and 183 GPa respectively. Smith *et al.* [15] performed MD simulation of uniaxial tension of polycrystalline tantalum columns (built by using Voronoi method) having average grain size of 20 nm at 300K. Their work suggested that the process of twin formation lags the process of dislocation nucleation. They observed that at lower strain rate (10^5 to 10^7 s^{-1}), screw dislocation emission is the initial deformation mechanism while at higher strain rate (>10^8 s^{-1}), deformation twinning prevails.

It may thus be seen that an ample amount of disparate literature exists reporting several important results on the deformation aspects of tantalum, some differing with each other. Most importantly, despite all these studies, there has been no effort made to clarify how nanoindentation of Ta is going to be influenced by its crystal orientation which mandated the need for this work.

3. Molecular dynamics simulation of nanoindentation

Molecular dynamics (MD) simulation is an appropriate choice to understand the atomistic tribology of simultaneously occurring processes, the foremost of which are structural transformations in the material, nucleation and propagation of dislocations and thermodynamics of the process. In this work, the “Large-scale atomic/molecular massively parallel simulator” (13

September 2013 version) [16] was used to perform a series of MD simulations. An Open Visualization tool (OVITO) [17] was used to visualize and analyze the atomistic simulation data while an automated "dislocation extraction algorithm" (DXA) [18] and a crystal analysis tool (CAT) [19] were used for automated identification of crystal defects, dislocation lines and their Burgers Vector from the output of the MD data. DXA and CAT in conjunction with OVITO provides unique flexibility to measure the length of dislocations in a fully automated fashion, an example may be seen elsewhere [20].

The MD simulation model after equilibration is shown in figure 2a. The atoms in the Newton region directly affected by the chemical interactions were allowed to follow Newtonian dynamics (LAMMPS NVE dynamics), while atoms in a thin boundary layer were subjected to a thermostat (LAMMPS NVT dynamics) to dissipate the heat generated in the artificial volume which would have otherwise taken away by the air during nanoindentation or lubricant (in cutting). Normally, pyramidal indenters, such as Berkovich or cube corner, are classified as ‘‘sharp’’ indenters while spherical indenters are referred to as ‘‘blunt’’ indenters [3]. In practice, almost all indenters have some finite edge radius (despite being referred to as extremely sharp) and therefore a spherical shaped indenter was deployed (figure 2a) during the simulation to mimic an indenter with a finite edge radius. However, the atoms in the indenter were kept fixed (the indenter was assumed to be an infinitely rigid body). In the literature, there wasn't any robust interaction potential energy function between carbon and tantalum (to the best of our knowledge) and hence, spherical indenter was filled with the tantalum atoms to describe the chemical interactions. While such an assumption is not novel [21], it was ensured prior to this study that our results on dislocation mechanics and yielding stresses are not out of order with such an assumption. Accordingly, we have performed an extensive stress and dislocation mechanics analysis and have found that this consideration can predict the Tresca yielding stress of the substrate to be in close proximity of what would have otherwise predicted by a rigid diamond indenter. We also performed an additional dummy trial with a different kind of indenter description. The selection of this kind of indenter was driven from the notion that the experimental conditions often involve the presence of oxide layers which creates a

passivation layer over the indenting surface. To mimic these conditions, Kelchner *et al.* [7] described a purely spherical repulsive rigid indenter with a force potential. As per this potential, each atom in the indented material interacts with the idealized indenter to experience a force of magnitude $F(r) = K(r-R)^2$ where *K* is the force constant (2 KeV/Å^3= 3204 nN/Å^2), *R* = 3 nm, radius of the spherical indenter and *r* is the distance of an atom of another species from the centre of the spherical indenter. This implies that F(r) remains repulsive as long as R > r and becomes zero otherwise. To check the sensitivity of the value of K on the nanoindentation results, an additional dummy trial was carried out by changing the value of *K* from 2 KeV/Å^3 to 1 KeV/Å^3 but the simulation results were found insensitive to the value of *K*. To avoid any artificial effect of the temperature (due to thermal fluctuations and thermal vibrations), a low temperature of 10 K was used to equilibrate the sample and to perform the nanoindentation. Choi *et al.* [22] have discussed some implications of the boundary conditions for such a simulation model and accordingly the model in this work sassumed periodic boundary conditions along X and Z directions (figure 2).

A myriad of potential energy functions for simulation of Ta have been proposed in the past [23-26]. In common with each other, most of these potential functions predict the yield behaviour of Ta associated with the slip of a single screw dislocation arising of a metastable dislocation core structure that naturally follows the (112) plane [27]. On studying the extensive literature on the list of potential energy functions for Ta, the angular dependent potential function of Mishin *et al.* [28] has been reported to agree well with the *ab-initio* calculations while the analytical Embedded-atom-method (EAM) potential proposed by Guellil *et al.* [29] shows 27% discrepancy between the calculated and experimental values of bulk modulus [30] of Ta. Smith *et al.* [15] noted that the EAM potential by Li *et al.* [30] has been rigorously researched by Alleman *et al.* [31], who find this potential function being robust in revealing elastic modulus, predictions of gamma surfaces, BCC screw dislocation core and unstable stacking fault energy barrier determined by density functional theory (DFT) calculations. However, a comparison across several potential functions [32] specifically compared to study the nanoindentation process suggests that the potential energy function proposed by Li *et al.* [30] poses some serious concerns on the simulation results and is

hence unreliable to study Ta under the conditions of high pressure.

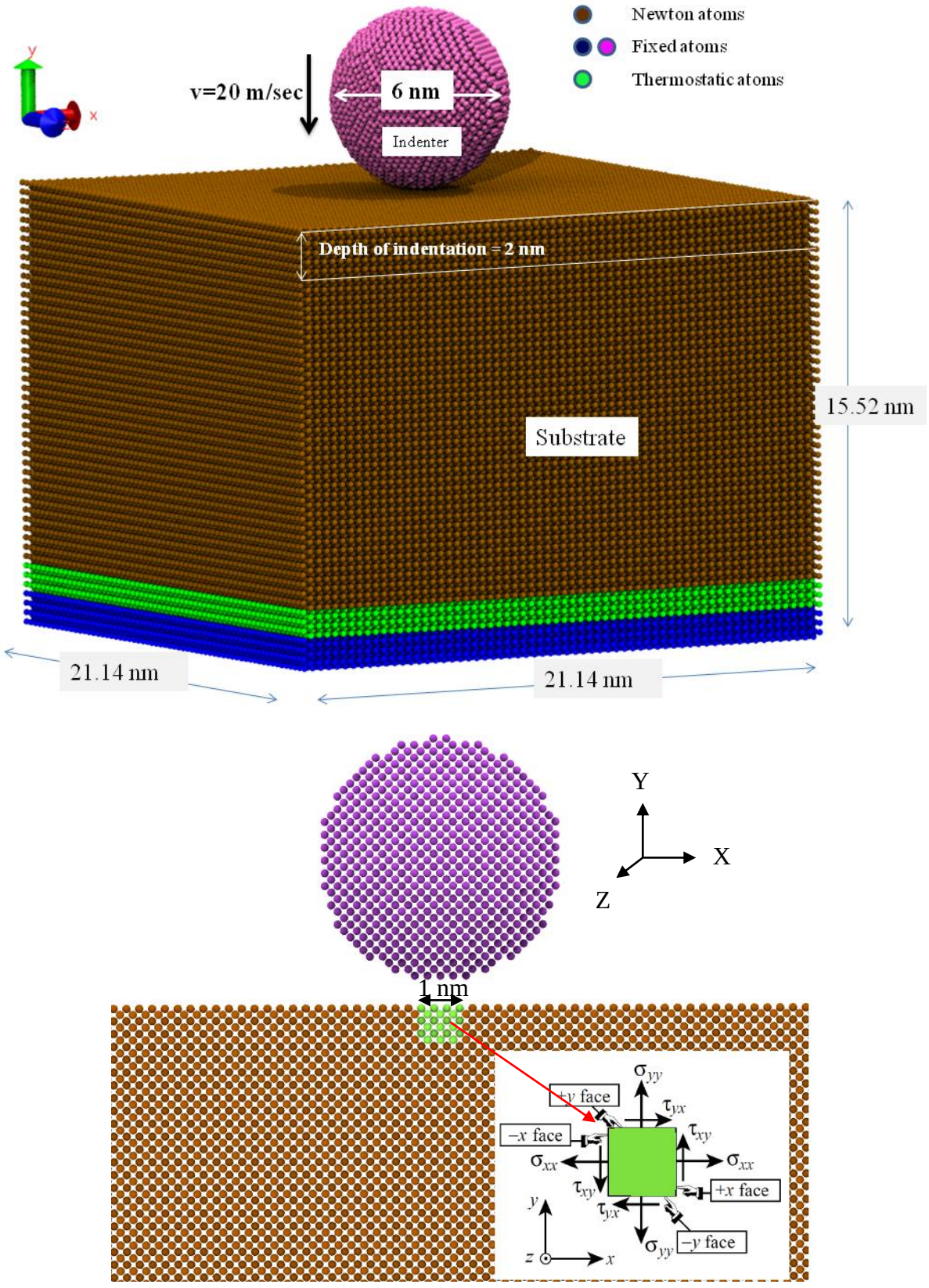

Figure 2: Schematic diagram (a) MD simulation model of the nanoindentation (b) volume of material (1nm×1nm×1nm) considered for stress computation (only 2D representation is shown here)

A recent study [32] compared several potential function and suggests an extended Finnis-Sinclair

potential function proposed by Dai *et al.* [26] to be least sensitive to indenter diameter and indentation velocity. On the other hand, the EAM potential function of Ravelo *et al.* [23] has been tested during nanoindentation [13] as well as shock compression experiments [23] and the outcome suggests that this potential function is better in predicting the high pressure and high temperature phases of Ta. Since the intent of this work is to understand the deformation behaviour of Ta, this study made use of an EAM potential (Ta-1) developed by Ravelo *et al.* [23] primarily to study extreme conditions of temperature and pressure such as during nanoindentation. While the details of all these potential functions are readily available from their respective sources, the details of the parameters used to develop the MD simulation model in this work are shown in Table II. The results reported here are very much reproducible, and these parameters may readily be used for replication of results.

Table II: Details used for development of the MD simulation model

Equilibrium parameter of tantalum	BCC material with a lattice constant of 3.304 Å	
Dimension of the tantalum workpiece	Crystal orientation	Number of atoms in the workpiece
21.136 nm × 15.52 nm × 21.136 nm	(010)	385024
21.033 nm × 15.41 nm × 21.165 nm	(110)	380952
21.033 nm × 15.44 nm × 21.018 nm	(111)	379080
Indenter specifications	6 nm diameter rigid spherical indenter (filled with Ta atoms) having (010) crystal orientation	
Description of indenter, workpiece and cross interactions (Potential energy function used)	EAM potential function [23]	
Indenter and specimen surface distance (initial)	0.5 nm	
Depth of indentation	2 nm	
Speed of indentation and retraction	20 m/s = 0.02 nm/ps	
Total simulation time (Indentation+retraction)	(2+0.5 nm)/0.02 nm/ps = 125 ps×2 = 250 ps	
Timestep for each calculation	2 fs = 0.002 ps	
Total run timesteps	250/0.002 = 1,25,000	
Boundary conditions	Periodic in X and Z direction	
Ensemble used in the simulation	NVE at 10 K	

The analysis of maximum shear stress or Tresca Stress in the deformation zone calls for quantifying the atomic stresses and for this reason, the atomic stress tensor[1] during the simulation was calculated by considering an elemental atomic volume (1 nm × 1 nm × 1 nm) in the deformation zone right underneath the indenter as shown in figure 2b. During the simulation, the summation of the total stresses acting on this small volume was divided by the pre-calculated total volume of the element to obtain the physical stress tensor. The physical stress tensor was then used to assess the yielding criteria of tantalum using Tresca stress, von Mises stress, Octahedral stresses, Principal stresses and hydrostatic stress using the equations shown in Appendix I. In addition to the yielding stresses, further analysis was carried out by estimating the contact pressure (p_m) underneath the indenter using the Oliver and Pharr method [33]. The details of the implementation of this method are described elsewhere and are not repeated here for brevity [2]. For better estimation, the parameters such as υ_s =0.32 (Poisson's ratio of Ta), υ_i =0.103 (Poisson's ratio of infinite rigid body (like diamond)), E_i = 1062.5 GPa (Young's modulus of diamond) were collected directly from the MD simulation.

3.0. Results and discussions

3.1. Testing of the potential energy function

Prior to carrying out the nanoindentation simulations in this work, the potential function was tested for its accuracy in reproducing the elastic constants and other important mechanical properties such as Zener anisotropy ratio, Young's modulus, shear modulus, Voigt Poisson's ratio and Voigt Bulk modulus at 0 K. These values are shown and compared with experiments in Table III for reference.

Table III: Experimental properties of tantalum compared with the MD simulation values

Properties of tantalum	**Obtained from Ta-1 EAM potential used in this study at 0 K [23]**	**Experimental values at 0 K [34]**
Equilibrium lattice constant **(Å)**	3.304	**3.3026**
C_{11} = C_{22} = C_{33} (GPa)	262.703	**266.32**

[1] http://lammps.sandia.gov/doc/compute_stress_atom.html

$C_{12} = C_{13} = C_{23}$ (GPa)	160.821	**158.16**
$C_{44} = C_{55} = C_{66}$ (GPa)	81.815	**87.36**
Zener anisotropy ratio $\frac{C_{11}-C_{12}}{2\times C_{44}}$	0.622	0.619
Young's modulus (E_{100}) [11] (GPa) $C_{11}-2\frac{C_{12}}{C_{11}+C_{12}}C_{12}$	140.57	148
Young's modulus (E_{110}) [11] (GPa) $4\frac{(C_{11}^{\ 2}+C_{12}C_{11}-2C_{12}^{\ 2})C_{44}}{2C_{44}C_{11}+C_{11}^{\ 2}+C_{12}C_{11}-2C_{12}^{\ 2}}$	190	201
Young's modulus (E_{111}) [11] (GPa) $3\frac{C_{44}(C_{11}+2C_{12})}{C_{11}+2C_{12}+C_{44}}$	215	228
Shear modulus(G) [35] (GPa) $\frac{C_{11}-C_{12}+C_{44}}{3}$	61.23	65
Voigt Poisson's ratio [35] $\frac{C_{11}+4C_{12}-2C_{44}}{4C_{11}+6C_{12}+2C_{44}}$	0.34	0.33
Voigt Bulk Modulus(B) (GPa) [36] $\frac{(C_{11}+C_{22}+C_{33})+2(C_{12}+C_{13}+C_{23})}{9}$	194.78	194

3.2. Analysis of dislocations and crystal defects in the Ta substrate

Indentation essentially consists of pressing a non-compliant indenter into the surface of the material to be investigated. The material can accommodate the indenter by elastic or plastic deformation, local cracking, nucleation of dislocations, phase transformations, or a combination of these accommodation mechanisms. Figure 3 shows the (convoluted looking) dislocation structures in the plastic zone of tantalum post indentation by a depth of 2 nm in all the three cases. The bottom portion of the figure shows the magnified view both at the peak indentation depth and after the indenter was retracted. Further details of these dislocations are provided in table IV. This data was used to estimate the dislocation density (m^2) in all the three simulation cases [37-38] using

$\text{Density of dislocations} = \text{Length of dislocations} / (2\pi R_{pl}^{3}/3) - (2\pi h^{3}/3)$ where R_{pl} is the radius of the plastic zone (largest distance of a dislocation from the indentation point) which is assumed to be hemispherical, and for an indentation depth of *R*, the indented volume is also considered hemispherical. Consequently, the dislocation density obtained from MD during indentation of Ta by 2 nm depth, was found to be of the order of **1.6×10^{14} m^{2}**.

(a)

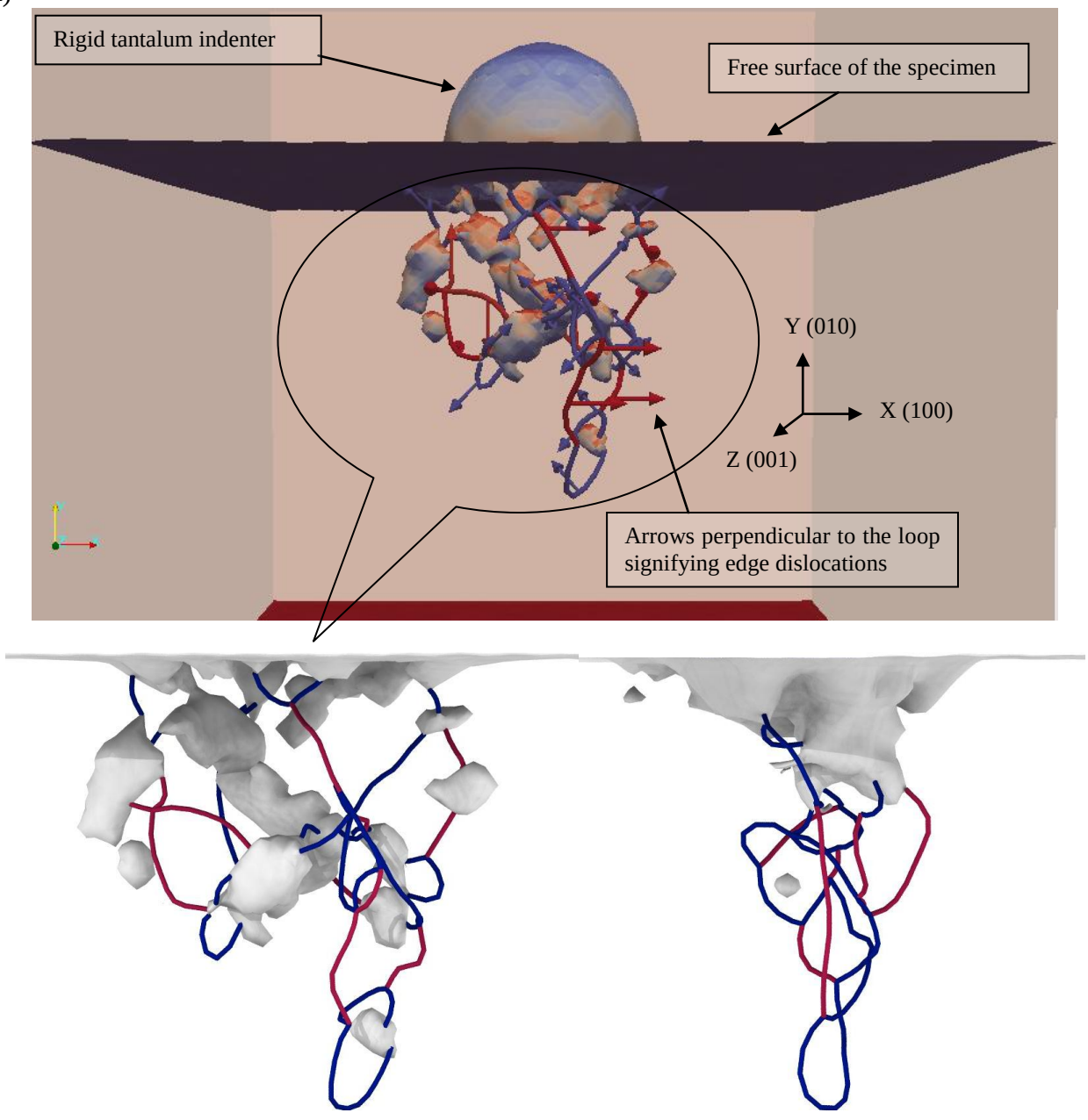

Upon loading by 2 nm

After complete unloading

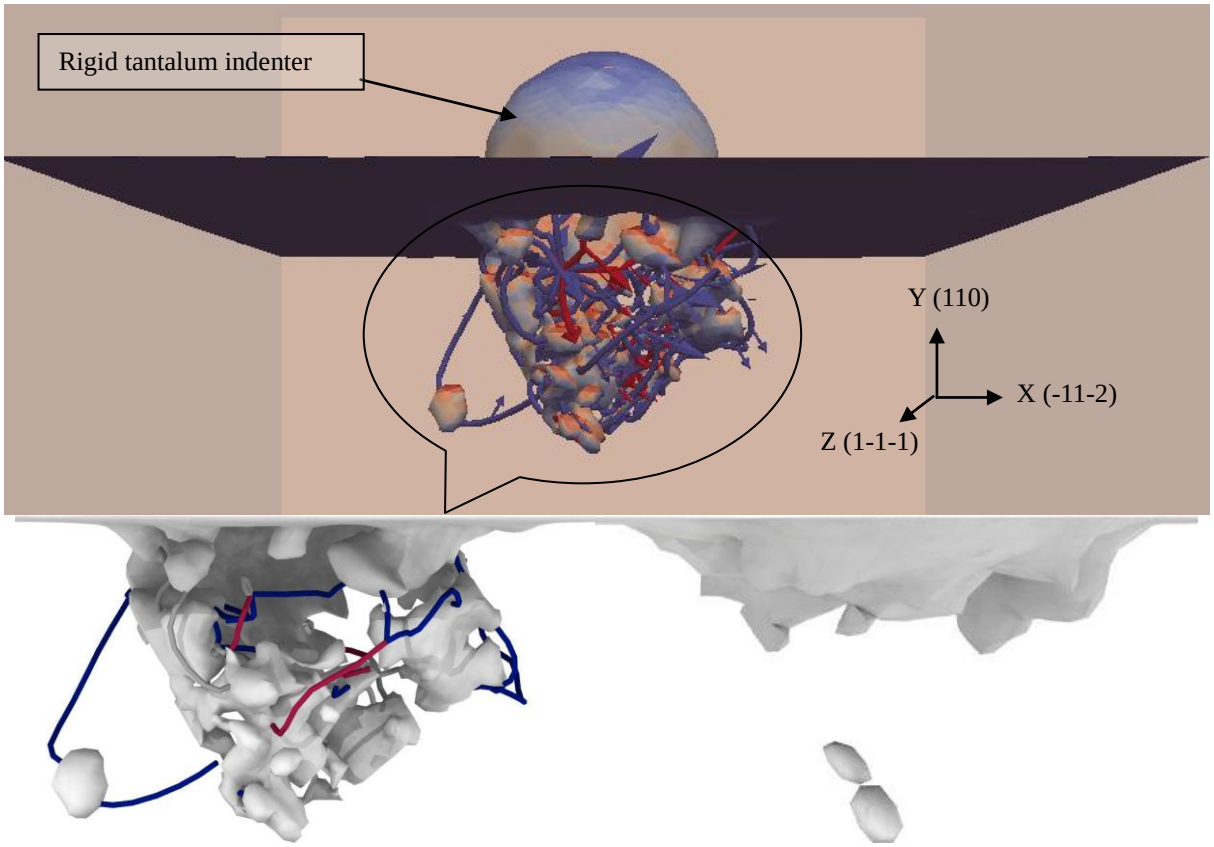

(b) Upon loading by 2 nm After complete unloading (no dislocations)

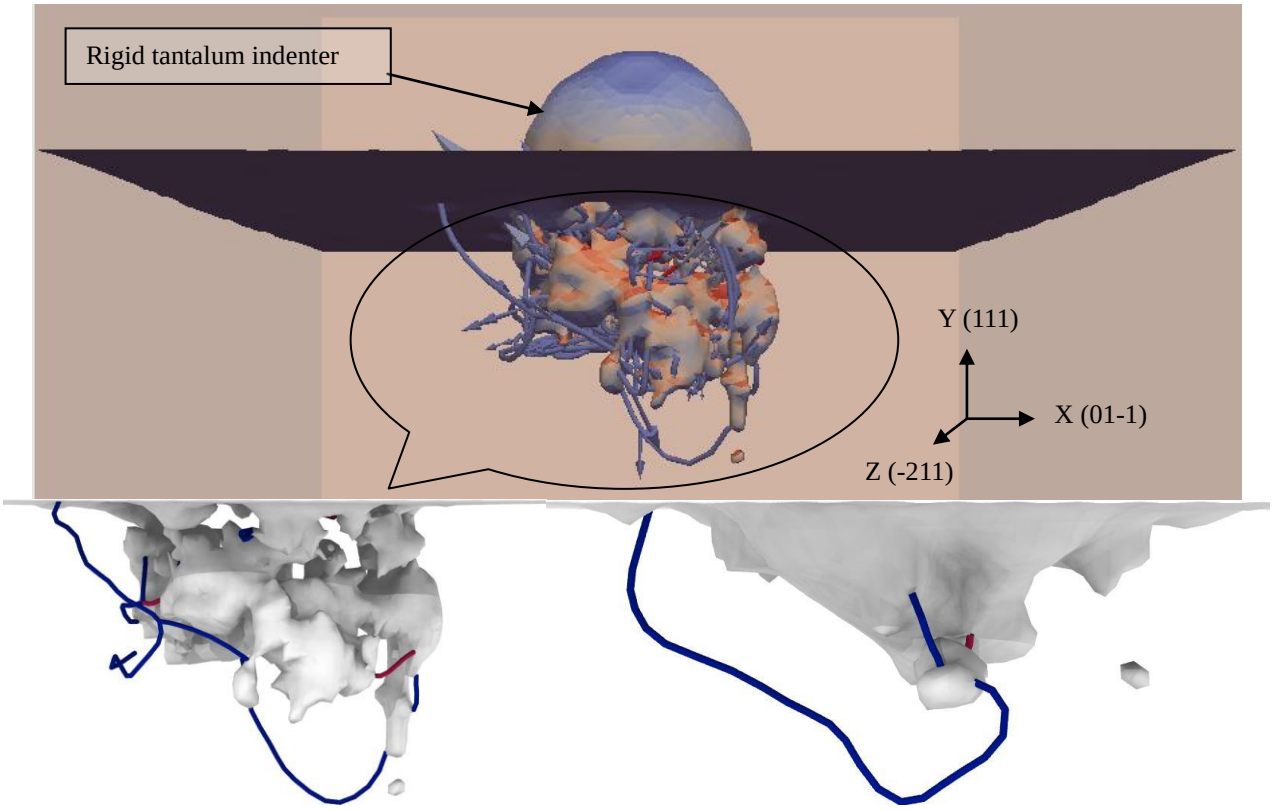

(c) Upon loading by 2 nm After complete unloading

Figure 3[2]: Output of the DXA showing plastic deformation zone, crystal defects, free surfaces and

[2] Readers are requested to refer the web based version of this article for correct interpretation of the colour legends

dislocation lines during nanoindentation of tantalum on three orientations (a) (010) orientation (b) (110) orientation and (c) (111) orientation. The geometric boundaries of tantalum are shown, while the geometric boundaries of the disordered phases are not visible in these visualizations. The top part shows the bulk view at peak loading conditions while the bottom part shows the magnified view of the plastic zone at peak loading and upon unloading. Dislocations with **b**=1/2<111> are shown in blue and **b**= <100> are shown in red. Arrows indicate the direction of **b** (Burgers Vector) with respect to the dislocation loop. Here these arrows are in a direction perpendicular to the dislocation lines signifying that the dislocations are pure edge dislocations.

Figure 3 also revealed that the prismatic dislocation loops were observed to transport the material downward under the wake of the indenter. Furthermore, Burgers vector of the dislocation lines (arrows shown in figure 3) were found perpendicular to the dislocation line, clearly indicating the edge nature of the dislocations rather than screw dislocations observed during tensile pulling [15] of Ta. There were two major types of dislocations captured with **b**=1/2<111> (blue colour) and **b**= <100> (red colour). On some instances, the <100> dislocation was found to form as a result of the interaction between two 1/2<111> dislocation loops. The inspection of the dislocation upon unloading revealed no dislocation on the (110) orientation unlike the (100) and (111) orientations meaning thereby that the plasticity on this orientation in particular is not only driven by dislocation nucleation.

Table IV: Characteristics of the dislocations obtained using the three simulation cases with rigid tantalum indenter. **L** is the total length of dislocations in Å

	(010) orientation	**(110) orientation**	**(111) orientation**
Burgers Vector (b=1/2<111>)			
L (total length) of dislocations	663.914 Å	763.899 Å	993.06 Å
Burgers Vector (b=<100>)			
L (total length) of dislocations	96.255 Å	149.3 Å	36.44 Å
Total length of dislocations	**760.17 Å**	**913.19 Å**	**1029.5 Å**
Radius of the plastic zone (R_{pl})	**131 Å**	**140 Å**	**145 Å**
h (displacement of the indenter)	**20 Å**	**20 Å**	**20 Å**
Dislocation density obtained from the MD simulation	**$1.62 \times 10^{14}\ m^2$**	**$1.59 \times 10^{14}\ m^2$**	**$1.615 \times 10^{14}\ m^2$**

Apart from prismatic dislocation loops, crystal defects in the form of twin boundaries below the indenter were also observed, these are highlighted in figure 4. In figure 4, the green coloured atoms refer to twin boundaries. It is noticeable that the twin boundaries (twin planes ((112) planes) (well known to be responsible for plasticity in BCC metals) were noticed only during indentation on the

(110) and (111) plane and not on the (010) plane when the indentation was performed with the rigid tantalum indenter. However, while the dummy indenter was used, the twin boundaries were observed on the (010) plane as well. This is one of those grey area where the use of a diamond indenter can verify the presence of twin boundaries during indentation on the (010) orientation of Ta. Further analysis using the CAT tool also revealed the presence of FCC atoms on the all the crystal planes which is likely on account of the fact that the local temperature of certain atoms underneath the indenter was more than 0.15 times the melting temperature of Ta.

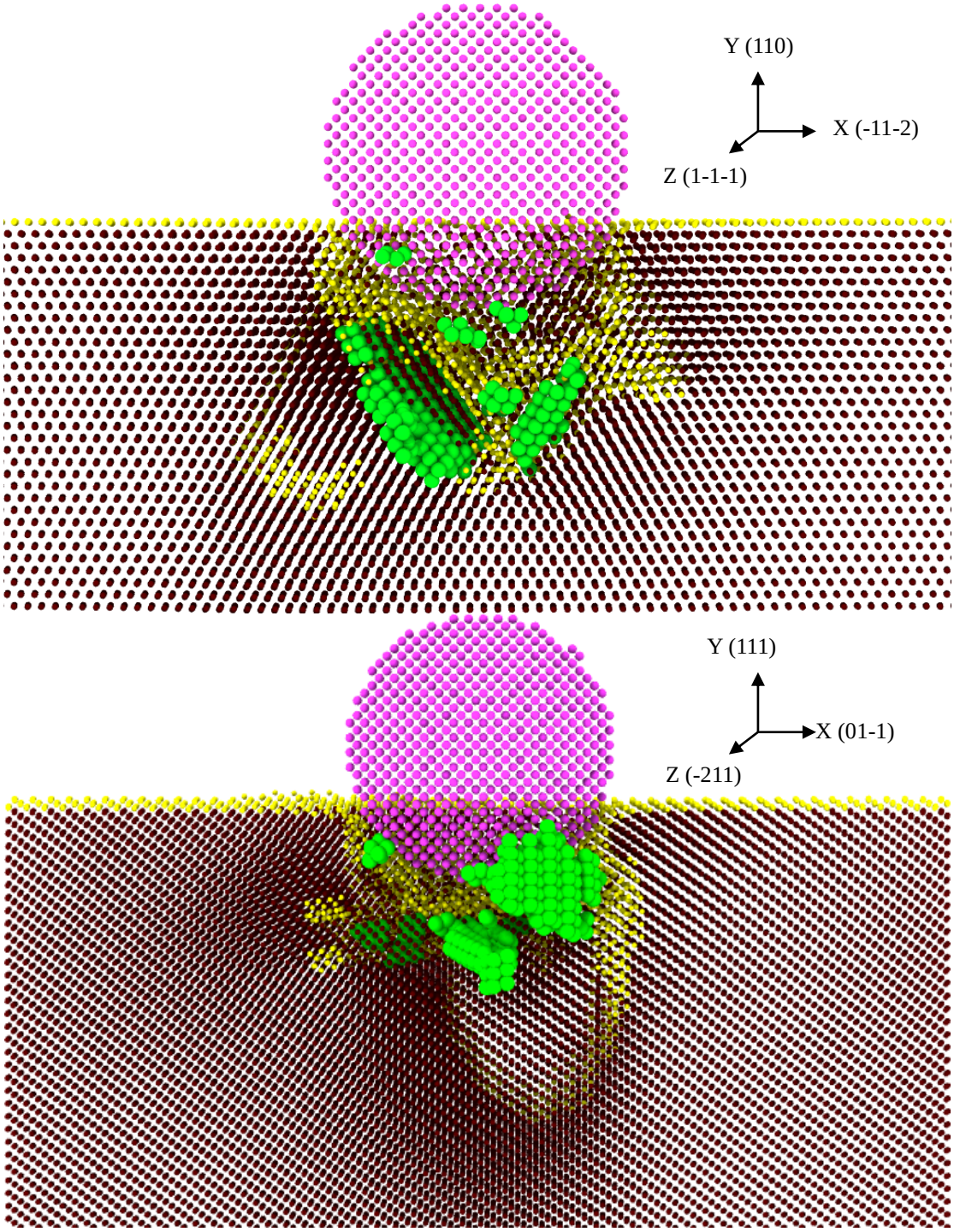

Figure 4: Spliced cross sectional views in the XY plane showing twinning on the (110) and (111) crystal orientations. No twin boundaries were detected on the (010) orientation. Common neighbour analysis (CNA) is used to identify and distinguish the crystalline atoms (shown in brown colour), atoms with crystalline defects are shown in yellow colour and rigid indenter is shown in pink colour. Green colour is used to mark atoms that form the twin boundaries in the entire substrate.

3.3. 3D stress analysis, maximum shear stress and pileup formation

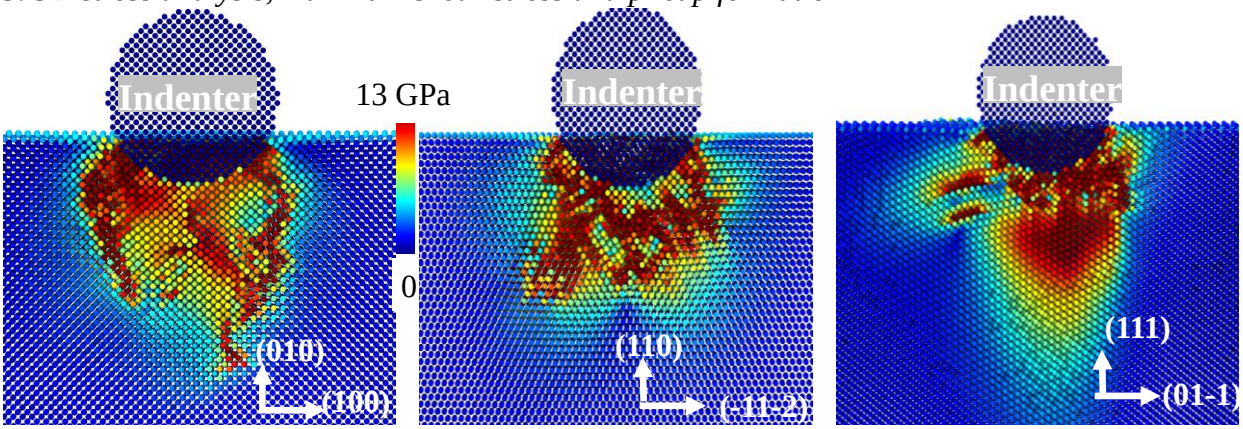

(a) View on the XY Plane (front view) showing variation in the octahedral shear stress on the three orientations of tantalum underneath the indenter obtained from the MD simulation

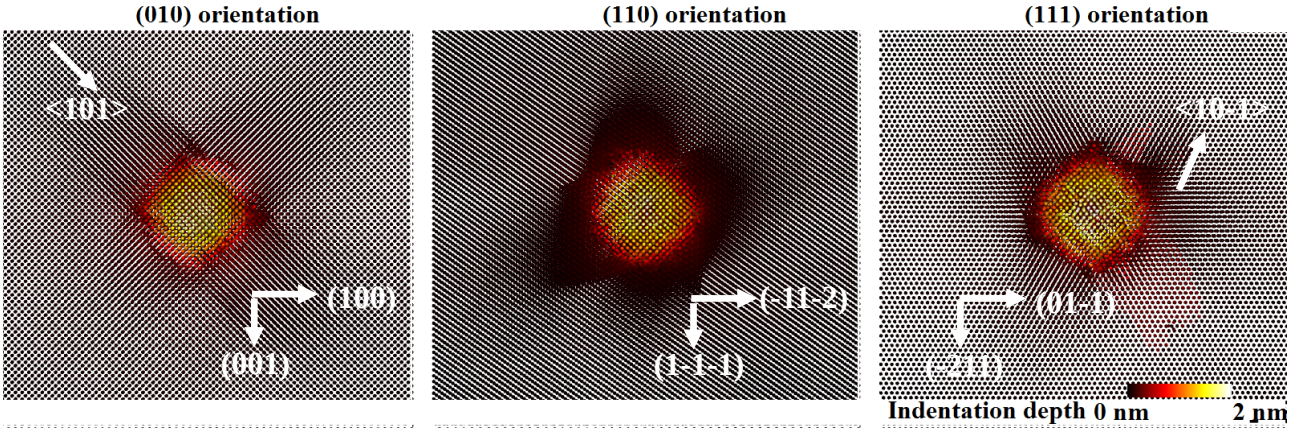

(b) View in the XZ plane (top view) showing atomic displacements (lattice deformation) on all three crystal planes of tantalum obtained from the MD simulation

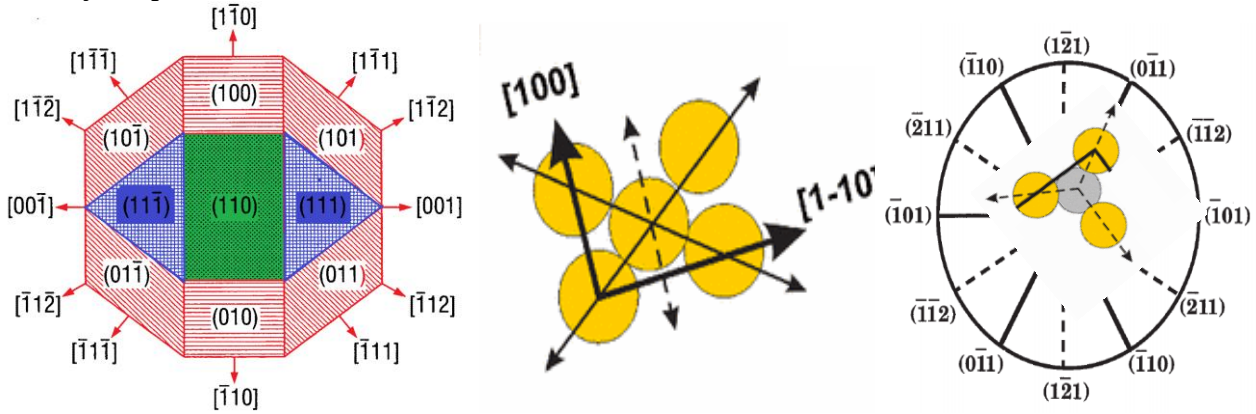

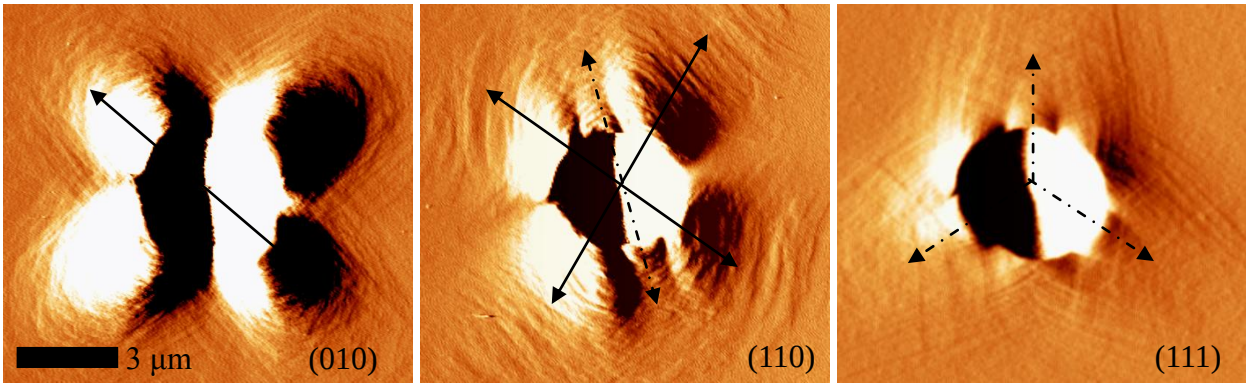

(c) Experimental results [1] obtained from nanoindentation on Ta on three different orientations

Figure 5: MD results compared with experiments (a) showing octahedral shear stress variation while (b) and (c) showing pile-up and lattice deformation along the closed packed directions

Table V: Nanoscale yielding stresses of tantalum obtained from the MD simulation

Critical value of maximum stress (GPa) in the deformation zone of tantalum	**(010) orientation**		**(110) orientation**	**(111) orientation**
	With a pure repulsive indenter	With a rigid tantalum indenter	With a rigid tantalum indenter	With a rigid tantalum indenter
Von Mises stress	28.69	21.94	10.05	12.51
Octahedral shear stress	13.52	10.34	4.74	5.9
Tresca stress	14.4	11.78	5.43	6.86
Major principal stress	-36.53	-30.66	-22.24	-30.05
Minor principal stress	-7.74	-7.09	-11.85	-16.85
Hydrostatic stress	-20.56	-25.74	-17.18	-24.52

Table VI: Ratio of mean pressure (p_m) to the Tresca stress or maximum shear stress

Value of sress (GPa)	**(010) orientation**		**(110) orientation**	**(111) orientation**
	With a pure repulsive indenter	With a rigid tantalum indenter	With a rigid tantalum indenter	With a rigid tantalum indenter
Shear strength of Ta (G/2π)	10.03	10.03	10.03	10.03
Tresca (T) or Maximum shear	14.4	11.78	5.43	6.86

stress in the deformation zone				
Mean pressure (p_m) (Instant force / Projected contact area)	14.48	14.17	14.13	16.13
Ratio of (T/p_m)	1	0.83	0.38	0.42

Figure 5(a) shows the sectional view in the XY plane representing the distribution of the octahedral shear stress during the deformation of tantalum on each of the three orientations when the indenter has moved into the substrate by 2 nm. Figure 5(b) on the other hand shows the spliced view in the XZ plane (top view) of the substrate in conjunction with figure 5(a) and compare the topography of the lattice deformation and pileup with figure 5(c) obtained from the experiments [1]. Interestingly, a very distinct distribution of octahedral shear stress is apparent which varies with its location during indentation on each plane. This could certainly be attributed to the differences in the BCC crystal structure and this difference leads to the deformation patterns to resemble as to what has been shown in figure 5(b). In figure 5(b), the simulations performed on the (010) orientation of Ta showed the pileup pattern (lattice deformation) along the closed packed direction of the BCC metal. Interestingly, in the case of the (110) orientation, where both in-plane and out-of-plane slip directions are available, the pileup is predominantly found along the in-plane slip directions resembling closer with the microscale experimental findings [1]. These results are incorporated in table V and it can be seen that the repulsive indenter overestimated the deformation stresses by a slight margin and later the *P-h* profile (figure 7) has also been compared where the repulsive indenter underestimated the peak load for the same amount of indenter displacement. The classical Hertzian contact theory suggests a multiplicative factor of 0.465 with the mean pressure to arrive at the maximum shear stress underneath the indenter [39]. This value is taken as a conventional wisdom in a variety of indentation studies and has somewhat become a common lore [1] particularly due to the fact that the direct measurement of maximum shear stress during the experiments is difficult. MD simulation results (table VI) clarify that this multiplicative factor from the classical Hertzian contact may be incorrect at the atomic scale. Table VI obtained from the MD

results shows (i) this ratio to be about 0.4 for the (110) and (111) orientation and ~0.8 for the (100) orientation of tantalum and (ii) the maximum shear (Tresca) stress was found to exceed the theoretical shear strength of tantalum on the (010) orientation but was well within for the (110) and (111) orientations. This unique observation on the (010) plane seems to be in accord with a recent study [6] where the elastic-plastic limit of Ta was observed to go past the theoretically predicted critical shear stress.

3.4. P-h plots and indentation size effect

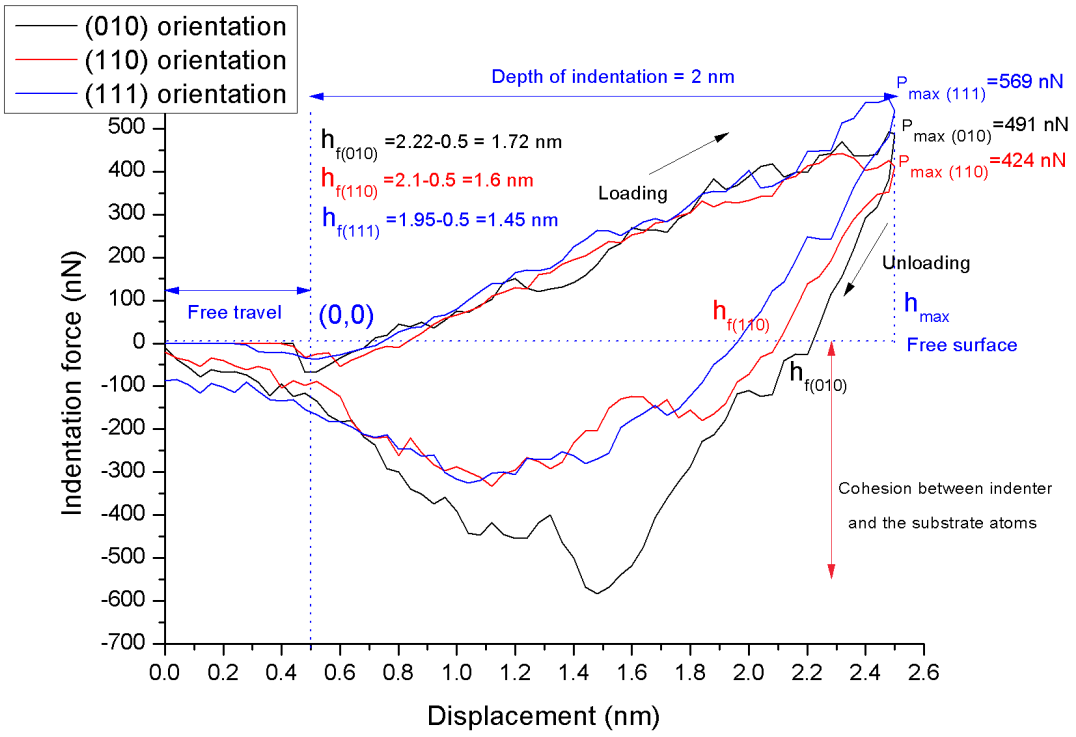

Figure 6: *P-h* plots obtained from the MD simulation for the three cases using rigid tantalum indenter

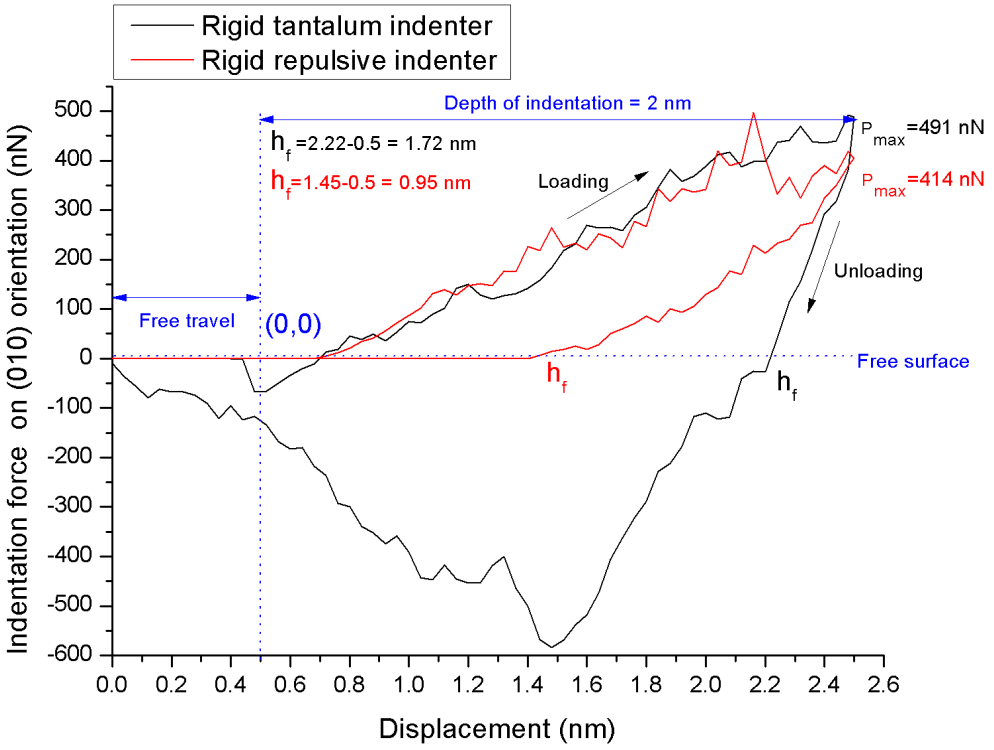

Figure 7: Comparison of *P-h* plots for indentation on the (010) orientation of tantalum by keeping all the indentation parameters same but using two different kind of indenters (i) using a rigid tantalum indenter and (ii) a purely repulsive indenter

A close examination of the *P-h* plots in figure 6 reveals clear differences in the force necessary to deform the three crystallographic orientation of tantalum to an indentation depth of 2 nm. The *P-h* plot for tantalum reveals that the indentation force (or energy) required to achieve a certain penetration depth in Ta is minimum on the (110) orientation and maximum on the (111) orientation while intermediate for the (010) orientation because the maximum load needed to indent the (111) orientation was much higher than what was needed to indent the (110) orientation. Also, it is quite surprising to see the cohesion component of forces during retraction stage. It appears that the (010) orientation has highest cohesion. However, it may be noted that the anisotropy for cohesion arises from the fact that a rigid tantalum indenter (010 orientation) was used for indentation meaning thereby that the same plane will have more cohesion. Thus, the cohesion anisotropic observations visible in these plots are something of an artefact which can better be confirmed using a diamond indenter. The slope or stiffness (*S*) of the unloading curves obtained from the MD simulation were 1617 N/m for the (010) orientation, 1375 N/m for the (110) orientation and 1611 N/m for the (111) orientation respectively signifying the stiffness of the system

for the three simulated crystal surfaces.

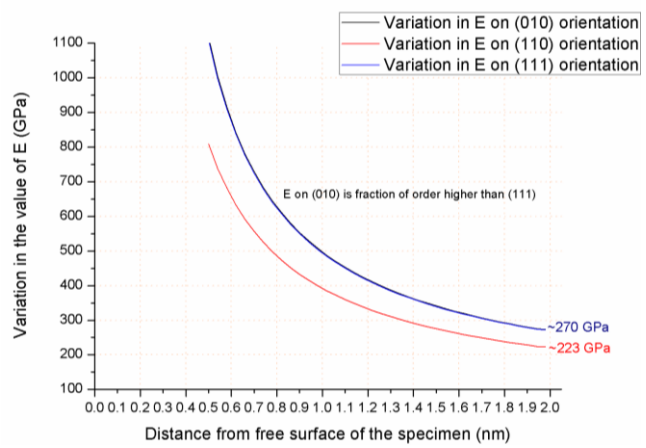

(a) Variation in the elastic modulus

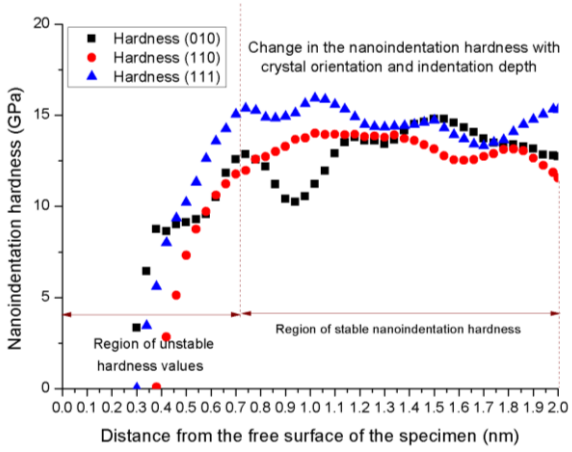

(b) Variation in the hardness

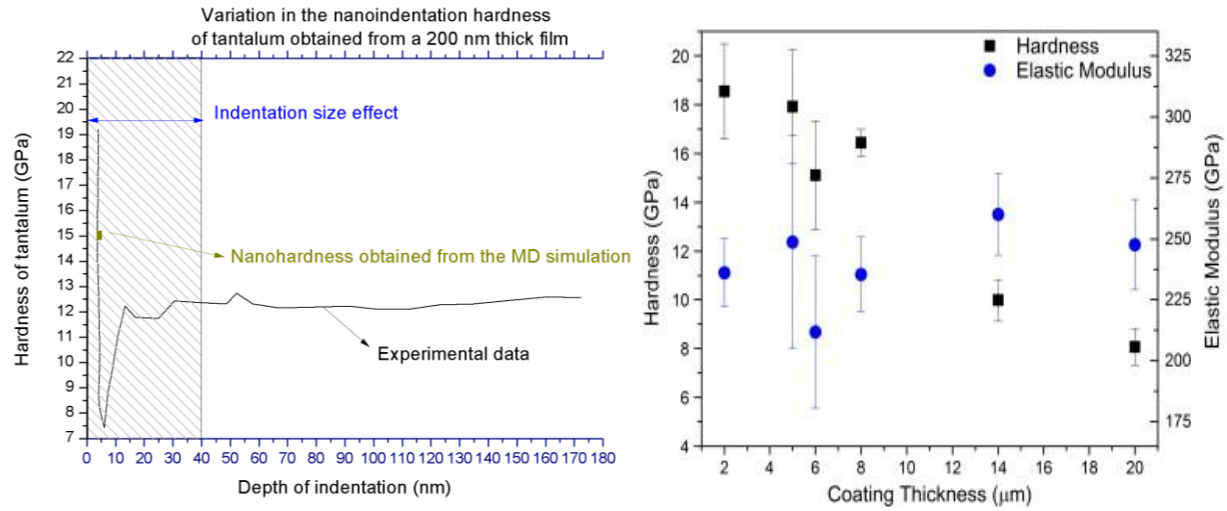

(c) Comparison of nanoindentation hardness between MD results and experiments [9, 40].

Figure 8(a): Variation in the elastic modulus (E) and 8(b) variation in the hardness (H) of tantalum with respect to the crystal orientation and indentation depth. Evaluation of E is shown after 0.5 nm of indentation depth while H variation is after 0.7 nm of indentation depth and 8(c) left part : size effect driven nanoindentation hardness of tantalum obtained from the experiments on 200 nm thick tantalum thin film is compared with the MD simulation value [40] at an indentation depth of 2 nm and a good agreement may be seen. 8c right part: The experimental results of the nanoindentation hardness and Young's modulus obtained by another research group [9] during a recent investigation matches the MD results quite closely.

The value of Young's modulus with the change in the crystal orientation and with the change in the indentation depth has been plotted in figure 8a and the corresponding hardness values are plotted in figure 8b. The hardness obtained from the MD data at the peak indentation depth of 2 nm is highlighted on the experimental scale obtained by indenting a thin film of tantalum by Guisbiers *et al.* [40] and Myers *et al.* [9]. Both experiments were done on the thin films of tantalum where the indentation depth is in few nanometres to sub-microns, a scale which is more close to compare with

MD values. It can be seen that the hardness and elastic modulus of tantalum obtained from the MD simulation by applying Oliver and Pharr method reveals very close value to what has been obtained through experiments in both cases. Both hardness [41-42] as well as Young's modulus [43] varies with size scale and the difference in the value of Young's modulus of tantalum on the (010) and (111) plane at 2 nm of depth of indentation was found subtle. The combined observation from figure 8(b) and 8(c) suggests that the indentation size effect driven hardness as well as the elastic modulus is quite high in tantalum compared to the bulk value of the same and that obtained from elastic constants of tantalum would suggest that the order of decreasing Young's modulus should be $E_{111} > E_{110} > E_{010}$. However, this was not the case as is evident from figure 8. Also, about 15 nm-40 nm depth is needed to get past the indentation size effect driven domain to get a more saturated value. The hardness values or the Hertzian stress underneath the indenter started stabilizing in all the three cases only after the indenter has moved by about 0.7 nm into the substrate making the hardness data calculated before this point meaningless [44]. Thus, around 0.7 nm of indentation depth is minimum needed indentation depth to get even the indentation size effect driven value of hardness. The indentation size effect in the hardness of BCC metals has been sub-divided into three regions [45], namely, Region-I, Region-II and Region-III which can be expressed as

$$H = \begin{cases} H_1 + l_1 h^{-n_1} & h > \delta_u \quad (\text{Region} - \text{I}) \\ H_2(l_2 - e^{-n_2 h}) & \delta_1 < h < \delta_u \quad (\text{Region} - \text{II}) \\ H_3 + l_3 h^{-n_3} & h < \delta_1 \quad (\text{Region} - \text{III}) \end{cases}$$

where H is material's hardness at micro or nanoscale, h is indentation depth, l_1,l_2 and l_3 are the material's length scale for region I, II and III respectively, H_1, H_2, H_3, n_1, n_2, n_3 are material constants while δ_u and δ_1 are the indentation depths that separate regions, I, II and III respectively. Furthermore, the variation in the hardness and elastic modulus of nanocrystalline metals (unlike polycrystalline materials) is well documented [40] and has been proposed to be described as $Hs = H + \frac{k_{H2}}{\sqrt{D}} + \frac{k_{H3}}{D}$ and $E_{Shape} = E\left(1 - \frac{\alpha_{shape}}{D}\right)$ where Hs is the size dependent hardness, H is the bulk hardness and K_{H2} and K_{H3} are the coefficients of a parabolic relationship between hardness vs $D^{-1/2}$, D is the grain size, E_{Shape} is the size dependent

Young's modulus and α_{shape} is the parameter quantifying the size effect.

Ibid. quoted Ao *et al.* [43] who proposed that the competition between the surface bond shrinkage and melting temperature variation with size reduction leads to the so called size effect in elastic modulus whereas Gu *et al.* [46] related this size-dependent behaviour to Debye temperature. The stabilized values of the Young's modulus suggest that the value of *E* on the (010) orientation is 0.02% higher than on the (111) orientation while the value of the (110) orientation is least. Analysing the hardness curve it appears that the (110) orientation shows the lowest hardness of the three orientations. Both observations are in accordance with the *P-h* plots wherein the (110) orientation showed the least steep unloading as well as loading slopes. These are quantified in table VII and the hardness value obtained by purely repulsive indenter has also been compared against the value predicted by the rigid tantalum indenter for reference. While both the values appears to be closer, the repulsive indenter predicts a more conservative value against what has been obtained from a rigid tantalum indenter. The residual depth of recovery was found to be least on the (111) plane and maximum on the (010) plane while intermittent on the (110) plane signifying the (111) orientation recovers more than the other two orientations. We also noted the peak temperature in the deformation zone which aligned with the above observations.

Table VII: Summary of results obtained from the MD simulation (P-h plots)

Crystal orientation	**Remarks**	**Peak Load (nN)**	**h_f (Residual depth of recovery) (nm)**	**Average hardness (GPa) as per Oliver and Pharr method [33]**	**Peak temperature in the deformation zone (K)**
(010)	Repulsive indenter	414	0.95	12.48	174
(010)	Rigid Tantalum indenter	491	1.72	14.17	206
(110)		424	1.6	14.13	133
(111)		569	1.45	16.13	180

The temperature in the deformation zone was found least while indenting on the (110) orientation.

The fact that screw dislocations in Ta are immobile at temperatures less than 493.5 K (0.15 T_{melt} of Ta) and that the temperature in the entire deformation zone is well below 493.5 K seems to augment strong support as to why no screw dislocations were observed in this study while prismatic dislocation loops signifying edge dislocations were only observed.

4. Comments on the future pathways of this work

The indentation contact behaviour of materials is characterised by combination of plastic, elastic-plastic deformation and fracture. However, there are two main approaches to the mechanics of indentation depending upon the whether the accommodation is by plastic deformation or by fracture. Considering the MD simulation, and if the contact force is applied to a material then constituent atoms will undergo reconfiguration from its original state, deforming the initial contact or near contact bonds in the process. If the bonds return to the original configuration as the applied load is unloaded, then the deformation is elastic. If however, the bonds stay deformed upon unloading then the deformation could be described as plastic. Thus, plastic deformation can be characterised by permanent displacements of atoms. However, if those few broken bonds are not reorganized then fracture can occur. The bulk material response under indentation is a function of the individual deformations of the bonds and can therefore be combination of elastic, elastic-plastic deformation and fracture. Since MD simulation is an important theoretical technique to understand the surface and sub-surface changes in materials, the current study has been motivated partly by the identification of initial stages of yielding and fracture mechanism, crystal defects, dislocation monitoring and differentiate the types of dislocation nucleation and its motion.

An improved understanding of the physical mechanisms underpinning the response of Ta during material property evaluation requires multi-scale approach integrating continuum and molecular dynamics (MD) theory. Although we have made advances in our understanding on some of the physical mechanisms, this is still a grey area. Since the term miniaturization has been coined, many classical phenomena's have undergone series of refinements owing primarily to the fact that the behaviour of material changes with the reduction in scale [47]. Apparently, the current canon of experimental facilities are not either easily available in public domain or are not sufficiently well

advanced to capture all the mechanisms (dislocation nucleation, motion, etc.), competing within the atomic scale regime. Consequently, the assemblage of knowledge from several disparate disciplines including chemistry, physics, material science, and computing science has resulted in the development of ever improving simulation techniques which are capable to capture these phenomena's to provide phenomenal insights of dislocation physics. The relationships among crystal orientation, dislocation nucleation and reactions and the resulting plasticity at nanoscale is a difficult bit to be understood by the state-of-the-art experimental studies alone. Detailed information on the atomic level changes leading to changes observed at macroscale can appropriately be obtained by MD simulation. In this work, a relatively simple yet an appropriate modelling approach using a simple EAM potential has provided pathways to understand the origins of twin boundaries and how it varies with the change in the indented surface of the same material (BCC tantalum). The potential to tap this effect can result in significant engineering applications and is an area which needs practical and experimental realization. Consequently, the purpose for which MD simulation was carried out in this work has provided the direction to use this knowledge in the experimental work; therefore there is an opportunity for developing richer theoretical models and at the same time the quantitative verification of the dislocation density is possible with the usage of transmission electron microscopy. Despite the fact that figure 8c offered useful insights on what may be expected by changing the indentation depth or the indenter diameter, figure 9 (nanoindentation results for silicon carbide) offer some insights on the variation in the Hertzian contact stresses with respect to the indentation load and edge radius of the indenter. These informations may readily be used to advance our understanding on the contact mechanics of tantalum as a function of shape of the indenter.

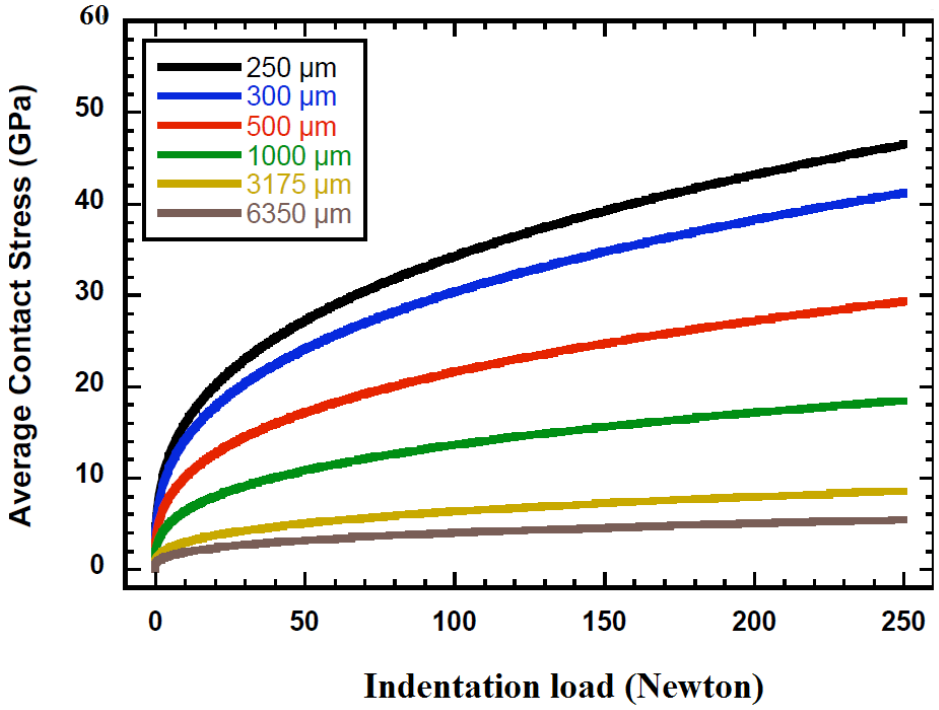

Figure 9: Variation in contact stresses with respect to indentation load and edge radius of the indenter [48]

Furthermore, the question whether the stress calculation should consider only single or a lump of atoms is yet to be answered. The procedure adapted in this work involved selecting a region right underneath the indenter having a volume of 1 nm^3 (almost equal to 60 to 70 atoms depending on the orientation of the substrate) in accordance with the previous studies [49]. A convergence study may be directed on the selection of this element size as a worthier future work.

The knowledge developed *via* this route will facilitate the process of theoretical developments leading towards the practical knowledge so as to avoid any future mishap. As tribological phenomena's depends heavily on the basic material properties in terms of microstructural variations, it may be possible to construct further models and to develop richer theoretical understanding linking mechanical parameters with material characteristics and its derived features. It also requires more research to bring out further improvements (both in testing, simulation and interpretation). To this end, this work provides an impetus for future work to find wider applications of Ta.

5. Conclusions

Using a force matching embedded atomic method (EAM) potential energy function driven molecular dynamics simulation in conjunction with crystal analysis tool, dislocation extraction algorithm, 3D stress analysis in the deformation zone and application of the Oliver and Pharr method, some novel and intriguing simulated nanoindentation results are obtained concerning crystal anisotropy of tantalum. Although the set of results can be summarized in length but for a ready glance, it can be seen for example that the elastic modulus obtained from elastic constants would suggest $E_{111} > E_{110} > E_{010}$. However, indentation simulation at depths of 2 nm and comparison with experiments shows that $E_{010} > E_{111} > E_{110}$. A couple of similarly striking results have been presented and discussed throughout the manuscript with the main conclusions to be drawn being:

1. The mechanism of the transport of material during nanoindentation and the observed plasticity in tantalum occurs due to the formation and motion of prismatic dislocations loops (edge dislocations) belonging to the 1/2<111> type, and <100> type Burgers vector family on all the three orientations and formation and migration of twin boundaries.

2. A unique and contrasting feature of the twin boundaries came to the observation was that upon retraction of the indenter on the (110) orientation, all the dislocations disappeared while the material did not fully recovered back (plastic response) suggesting twinning to be dominant over dislocation nucleation in driving plasticity in tantalum during nanoindentation.

3. It was found out that the maximum shear stress (critical Tresca stress) in the deformation zone exceeded the theoretical shear strength of tantalum (Shear modulus/2π~10.03 GPa) on the (010) orientation but was under the theoretical limit on the (110) and the (111) orientations. In light to this, the simulations strongly suggest that the conventional assumption that the maximum shear stress is simply 0.465 times the mean contact pressure breaks down at the atomic scale.

Acknowledgments:

The first author (SG) acknowledges the funding support from the International Research Fellowship account of Queen's University, Belfast in undertaking this work. The authors also acknowledge the

use of the HPC resources of STFC Hartree Centre, UK.

References

1. Biener, M.M., et al., *Dislocation nucleation in bcc Ta single crystals studied by nanoindentation.* Physical Review B, 2007. **76**(16): p. 165422.
2. Goel, S., et al., *Nanoindentation of polysilicon and single crystal silicon: Molecular dynamics simulation and experimental validation.* Journal of Physics D: Applied Physics, 2014. **47**(27): p. 275304.
3. Goel, S., et al., *Incipient plasticity in 4H-SiC during quasistatic nanoindentation.* Journal of the Mechanical Behavior of Biomedical Materials, 2014. **34**: p. 330-337.
4. Healy, C.J. and G.J. Ackland, *Molecular dynamics simulations of compression–tension asymmetry in plasticity of Fe nanopillars.* Acta Materialia, 2014. **70**(0): p. 105-112.
5. Wang, Y., et al., *Deformation twinning during nanoindentation of nanocrystalline Ta.* Applied Physics Letters, 2005. **86**(10): p. 101915.
6. Guerrero, O. and M. Marucho, *Elastic-Plastic Transition under Uniaxial Stress BCC Tantalum.* Journal of Materials Science and Engineering B, 2013. **3**(3): p. 153-160.
7. Kelchner, C.L., S.J. Plimpton, and J.C. Hamilton, *Dislocation nucleation and defect structure during surface indentation.* Physical Review B, 1998. **58**(17): p. 11085.
8. Cao, Z., et al., *The rate sensitivity and plastic deformation of nanocrystalline tantalum films at nanoscale.* Nanoscale Research Letters, 2011. **6**(1): p. 1-6.
9. Myers, S., et al., *The β to α phase transition of tantalum coatings deposited by modulated pulsed power magnetron sputtering.* Surface and Coatings Technology, 2013. **214**(0): p. 38-45.
10. Knepper, R. and S.P. Baker, *Coefficient of thermal expansion and biaxial elastic modulus of β phase tantalum thin films.* Applied Physics Letters, 2007. **90**(18): p. 181908-181908-3.
11. Goel, S., et al., *Anisotropy of single-crystal 3C–SiC during nanometric cutting.* Modelling and Simulation in Materials Science and Engineering, 2013. **21**(6): p. 065004.
12. Wang, G., et al., *Molecular dynamics simulations of 1/2 {1 1 1} screw dislocation in Ta.* Materials Science and Engineering: A, 2001. **309**: p. 133-137.
13. Remington, T., et al., *Plastic deformation in nanoindentation of tantalum: A new mechanism for prismatic loop formation.* Acta Materialia, 2014. **78**: p. 378-393.
14. Tang, Y., E.M. Bringa, and M.A. Meyers, *Inverse Hall–Petch relationship in nanocrystalline tantalum.* Materials Science and Engineering: A, 2013. **580**: p. 414-426.
15. Smith, L., et al., *Molecular dynamics study of deformation and fracture in a tantalum nano-crystalline thin film.* Modelling and Simulation in Materials Science and Engineering, 2014. **22**(4): p. 045010.
16. Plimpton, S., *Fast Parallel Algorithms for Short-Range Molecular Dynamics.* Journal of Computational Physics, 1995. **117**: p. 1-19.
17. Stukowski, A., *Visualization and analysis of atomistic simulation data with OVITO–the Open Visualization Tool.* Modelling and Simulation in Materials Science and Engineering, 2010. **18**(1).
18. Stukowski, A., V.V. Bulatov, and A. Arsenlis, *Automated identification and indexing of dislocations in crystal interfaces.* Modelling and Simulation in Materials Science and Engineering, 2012. **20**(8): p. 085007.
19. Stukowski, A. and K. Albe, *Extracting dislocations and non-dislocation crystal defects from atomistic simulation data.* Modelling and Simulation in Materials Science and Engineering, 2010. **18**(8): p. 085001.
20. Goel, S., *A topical review on "The current understanding on the diamond machining of silicon carbide".* Journal of Physics D: Applied Physics, 2014. **47**(24): p. 243001.
21. Hagelaar, J., et al., *Atomistic simulations of the formation and destruction of nanoindentation contacts in tungsten.* Physical Review B, 2006. **73**(4): p. 045425.
22. Choi, Y., et al., *Size effects on the onset of plastic deformation during nanoindentation of*

thin films and patterned lines. Journal of Applied Physics, 2003. **94**(9): p. 6050-6058.
23. Ravelo, R., et al., *Shock-induced plasticity in tantalum single crystals: Interatomic potentials and large-scale molecular-dynamics simulations.* Physical Review B, 2013. **88**(13): p. 134101.
24. Daw, M.S. and M.I. Baskes, *Embedded-atom method: Derivation and application to impurities, surfaces, and other defects in metals.* Physical Review B, 1984. **29**(12): p. 6443-6453.
25. Ackland, G. and R. Thetford, *An improved N-body semi-empirical model for body-centred cubic transition metals.* Philosophical Magazine A, 1987. **56**(1): p. 15-30.
26. Dai, X.D., et al., *Extended Finnis-Sinclair potential for bcc and fcc metals and alloys.* Journal of Physics: Condensed Matter, 2006. **18**(19): p. 4527.
27. Hale, L.M., J.A. Zimmerman, and C.R. Weinberger, *Simulations of bcc tantalum screw dislocations: Why classical inter-atomic potentials predict (112) slip.* Computational Materials Science, 2014. **90**(0): p. 106-115.
28. Mishin, Y. and A.Y. Lozovoi, *Angular-dependent interatomic potential for tantalum.* Acta Materialia, 2006. **54**(19): p. 5013-5026.
29. Guellil, A. and J. Adams, *The application of the analytic embedded atom method to bcc metals and alloys.* Journal of Materials Research, 1992. **7**(03): p. 639-652.
30. Li, Y., et al., *Embedded-atom-method tantalum potential developed by the force-matching method.* Physical Review B, 2003. **67**(12): p. 125101.
31. Alleman, C., et al., *Evaluating the effects of loading parameters on single-crystal slip in tantalum using molecular mechanics.* Philosophical Magazine, 2013. **94**(1): p. 92-116.
32. Ruestes, C.J., et al., *Atomistic simulation of tantalum nanoindentation: Effects of indenter diameter, penetration velocity, and interatomic potentials on defect mechanisms and evolution.* Materials Science and Engineering: A, 2014. **613**(0): p. 390-403.
33. Oliver, W.C. and G.M. Pharr, *Improved technique for determining hardness and elastic modulus using load and displacement sensing indentation experiments.* Journal of Materials Research, 1992. **7**(6): p. 1564-1583.
34. Featherston, F.H., *The Elastic Constants of Tantalum Tungsten and Molybdenum*, in *Physics*. 1963, United States Naval Postgraduate School: California.
35. Yamakov, V.I., et al., *Investigation of crack tip dislocation emission in aluminum using multiscale molecular dynamics simulation and continuum modeling.* Journal of the Mechanics and Physics of Solids, 2014. **65**(0): p. 35-53.
36. Hill, R., *The Elastic Behaviour of a Crystalline Aggregate.* Proceedings of the Physical Society. Section A, 1952. **65**(5): p. 349.
37. Wang, B., Y. Gao, and H.M. Urbassek, *Microstructure and magnetic disorder induced by nanoindentation in single-crystalline Fe.* Physical Review B, 2014. **89**(10): p. 104105.
38. Gao, Y., C.J. Ruestes, and H.M. Urbassek, *Nanoindentation and nanoscratching of iron: Atomistic simulation of dislocation generation and reactions.* Computational Materials Science, 2014. **90**(0): p. 232-240.
39. Grau, P., D. Lorenz, and A. Zeckzer, *Fundamentals of dislocation nucleation at nanoindentation.* Radiation Effects and Defects in Solids, 2002. **157**(6-12): p. 863-869.
40. Guisbiers, G., et al., *Fracture toughness, hardness, and Young's modulus of tantalum nanocrystalline films.* Applied Physics Letters, 2010. **97**(14): p. 143115.
41. Cao, Y., et al., *Nanoindentation measurements of the mechanical properties of polycrystalline Au and Ag thin films on silicon substrates: Effects of grain size and film thickness.* Materials Science and Engineering: A, 2006. **427**(1–2): p. 232-240.
42. Cao, Z., et al., *Indentation size effects on the creep behavior of nanocrystalline tetragonal Ta films.* Scripta Materialia, 2009. **60**(6): p. 415-418.
43. Ao, Z.M., S. Li, and Q. Jiang, *The determination of Young's modulus in noble metal nanowires.* Applied Physics Letters, 2008. **93**(8): p. -.
44. Chen, S. and F. Ke, *MD simulation of the effect of contact area and tip radius on nanoindentation.* Science in China Series G: Physics, Mechanics and Astronomy, 2004.

47(1): p. 101-112.
45. Voyiadjis, G.Z., A.H. Almasri, and T. Park, *Experimental nanoindentation of BCC metals.* Mechanics Research Communications, 2010. **37**(3): p. 307-314.
46. Gu, M.X., et al., *Size, temperature, and bond nature dependence of elasticity and its derivatives on extensibility, Debye temperature, and heat capacity of nanostructures.* Physical Review B, 2007. **75**(12): p. 125403.
47. Geim, A.K. and K.S. Novoselov, *The rise of graphene.* Nature Materials, 2007. **6**(3): p. 183-191.
48. Wereszczak, A. and K. Johanns, *SPHERICAL INDENTATION OF SiC.* Advances in Ceramic Armor II, Ceramic Engineering and Science Proceedings, Cocoa Beach, 2009. **314**: p. 43.
49. Goel, S., et al., *Diamond machining of silicon: A review of advances in molecular dynamics simulation.* International Journal of Machine Tools and Manufacture, 2015. **88**(0): p. 131-164.

APPENDIX - 1

$$\text{Stress tensor} = \begin{bmatrix} \sigma_{xx} & \tau_{xy} & \tau_{xz} \\ \tau_{xy} & \sigma_{yy} & \tau_{yz} \\ \tau_{xz} & \tau_{xz} & \sigma_{zz} \end{bmatrix} \quad (1)$$

Invariants:

$$I_1 = \sigma_{xx} + \sigma_{yy} + \sigma_{zz} \quad (2)$$

$$I_2 = \sigma_{xx}\sigma_{yy} + \sigma_{yy}\sigma_{zz} + \sigma_{zz}\sigma_{xx} - \tau_{xy}^2 - \tau_{xz}^2 - \tau_{yz}^2 \quad (3)$$

$$I_3 = \sigma_{xx}\sigma_{yy}\sigma_{zz} + 2(\tau_{xy}\tau_{yz}\tau_{xz}) - \tau_{xz}^2\sigma_{yy} - \tau_{yz}^2\sigma_{xx} - \tau_{xy}^2\sigma_{zz} \quad (4)$$

$$A_1 = -I_1 ; \quad A_2 = I_2 \quad A_3 = -I_3 \quad (5)$$

$$Q = \frac{3A_2 - A_1^2}{9} \quad (6)$$

$$R = \frac{9A_1A_2 - 27A_3 - 2A_1^3}{54} \quad (7)$$

$$D = Q^3 + R^2 \quad (8)$$

If $D < 0$ then as follows: else the condition is 2D stress

$$\theta = \cos^{-1}\left(\frac{R}{\sqrt{-Q^3}}\right) \quad (9)$$

$$R_1 = 2\sqrt{-Q} \times \cos\left(\frac{\theta}{3}\right) - \frac{A_1}{3} \tag{10}$$

$$R_2 = 2\sqrt{-Q} \times \cos\left(\frac{\theta + 4\pi}{3}\right) - \frac{A_1}{3} \tag{11}$$

$$R_3 = 2\sqrt{-Q} \times \cos\left(\frac{\theta + 2\pi}{3}\right) - \frac{A_1}{3} \tag{12}$$

$$\sigma_1 = \max(R_1, R_2, R_3) \quad \text{and} \quad \sigma_3 = \min(R_1, R_2, R_3) \tag{13}$$

$$\sigma_{\text{tresca}} = \frac{\sigma_1 - \sigma_3}{2} \tag{14}$$

$$\sigma_{\text{von Mises}} = \sqrt{\frac{(\sigma_{xx} - \sigma_{yy})^2 + (\sigma_{yy} - \sigma_{zz})^2 + (\sigma_{zz} - \sigma_{xx})^2 + 6(\tau_{xy}^2 + \tau_{yz}^2 + \tau_{zx}^2)}{2}} \tag{15}$$

$$\sigma_{\text{octahedral}} = \frac{\sqrt{(\sigma_{xx} - \sigma_{yy})^2 + (\sigma_{yy} - \sigma_{zz})^2 + (\sigma_{zz} - \sigma_{xx})^2 + 6(\tau_{xy}^2 + \tau_{yz}^2 + \tau_{zx}^2)}}{3} = \frac{\sqrt{2}}{3}\sigma_{\text{von Mises}} \tag{16}$$

$$\sigma_{\text{hydrostatic}} = \frac{\sigma_{xx} + \sigma_{yy} + \sigma_{zz}}{3} \tag{17}$$